

Formation and impact of nanoscopic oriented phase domains in electrochemical crystalline electrodes

Received: 14 May 2022

Accepted: 7 September 2022

Published online: 24 October 2022

 Check for updates

Wenxiang Chen^{1,2}, Xun Zhan^{1,2}, Renliang Yuan¹, Saran Pidaparthi¹, Adrian Xiao Bin Yong^{1,2}, Hyosung An^{1,2}, Zhichu Tang¹, Kaijun Yin¹, Arghya Patra^{1,2}, Heonjae Jeong³, Cheng Zhang⁴, Kim Ta^{5,6}, Zachary W. Riedel^{1,2}, Ryan M. Stephens⁷, Daniel P. Shoemaker^{1,2}, Hong Yang^{2,4,5}, Andrew A. Gewirth^{2,5,6}, Paul V. Braun^{1,2,3,4,5,8}, Elif Ertekin^{2,3}, Jian-Min Zuo^{1,2}  and Qian Chen^{1,2,4,5,8} 

Electrochemical phase transformation in ion-insertion crystalline electrodes is accompanied by compositional and structural changes, including the microstructural development of oriented phase domains. Previous studies have identified prevalently transformation heterogeneities associated with diffusion- or reaction-limited mechanisms. In comparison, transformation-induced domains and their microstructure resulting from the loss of symmetry elements remain unexplored, despite their general importance in alloys and ceramics. Here, we map the formation of oriented phase domains and the development of strain gradient quantitatively during the electrochemical ion-insertion process. A collocated four-dimensional scanning transmission electron microscopy and electron energy loss spectroscopy approach, coupled with data mining, enables the study. Results show that in our model system of cubic spinel MnO_2 nanoparticles their phase transformation upon Mg^{2+} insertion leads to the formation of domains of similar chemical identity but different orientations at nanometre length scale, following the nucleation, growth and coalescence process. Electrolytes have a substantial impact on the transformation microstructure ('island' versus 'archipelago'). Further, large strain gradients build up from the development of phase domains across their boundaries with high impact on the chemical diffusion coefficient by a factor of ten or more. Our findings thus provide critical insights into the microstructure formation mechanism and its impact on the ion-insertion process, suggesting new rules of transformation structure control for energy storage materials.

Understanding the development of transformation microstructures in crystalline solids is critical for advancement in materials engineering^{1–3}. The fine microstructures formed by the arrangement of phases in specific orientations—oriented phase domains—govern the materials'

physical and mechanical properties. Such transformation microstructures are widely found in phase-transforming solids when the symmetry of the matter changes, and are essential for strengthening by nanoprecipitates in aluminium or other alloys², shape memory from

A full list of affiliations appears at the end of the paper.  e-mail: jianzuo@illinois.edu; qchen20@illinois.edu

twinning martensites in shape memory alloys⁴, switching of oriented domains in ferroelectrics⁵ and so on⁶.

Transformation microstructure is also expected in the cycling of several widely adopted cathode materials, in which a multitude of phase transformations and phase symmetries have been reported, such as cubic-to-tetragonal phase transition in spinel structures^{7–9}, rhombohedral-to-monoclinic transition in layered oxides^{10–14} and the spinel structure formed in layered oxides^{8,15}. However, the nature and importance of oriented phase domains in crystalline electrode materials incurred during the electrochemically driven phase transformation are much less explored^{16–18}, despite recent studies suggesting the existence of ordered phases in layered electrodes^{10–14,19,20} and spinel structure^{8,21} on the basis of theoretical calculations¹⁴, electron diffraction^{11,12,18,19} and high-resolution electron microscopy^{8,16,20}. Previous research on electrochemical phase transformation has largely focused on nanoscale electrochemical inhomogeneity in composition and the associated strain in ion-insertion electrodes^{22–27}, using methods such as synchrotron-based microscopy at the length scale of tens of nanometres^{28,29} and analytical transmission electron microscopy^{30–32}. Such composition heterogeneity has been attributed to diffusion- or reaction-limited mechanisms³³ (Supplementary Note 1). For example, in a reaction-limited process the composition heterogeneity of Li_xFePO_4 platelet particles was observed to be suppressed on discharge and amplified on charge²², while upon diffusion limitation Li_xFePO_4 particles were found to form a phase-separated ‘sandwiched’ structure³⁴. Such composition heterogeneity can be minimized when the size of cathode particles is at the nanoscale due to a ‘nanosizing’ effect³⁵ or when they are cycled at a sufficiently high rate²². In comparison, the heterogeneity associated with the change in phase symmetries during phase transformation has received scant attention.

In this Article we elucidate the formation and evolution of oriented phase domains in cathode nanoparticles (NPs) during electrochemical phase transformation. Their detection and mapping at nanometre resolution are made possible by using a data-mining approach developed for four-dimensional scanning transmission electron microscopy (4D-STEM). Our model cathode of $\lambda\text{-MnO}_2$ NPs transforms from the high-symmetry cubic spinel structure ($Fd\bar{3}m$) to low-symmetry tetragonal phase ($I4_1/amd$) upon Mg^{2+} ion insertion, with one of the principal axes of the cubic spinel unit cell substantially strained ($\sim 15\%$)⁹. Collocated 4D-STEM and electron energy loss spectroscopy (EELS) shows that transformation microstructure forms in the NPs for a wide range of current rates, while the NPs promote a solid-solution-type phase transition according to X-ray diffraction (XRD). These oriented phase domains are observed to nucleate, grow and coalesce during the discharge process, with morphologies ranging from continuous ‘islands’ of about 20–50 nm to small, discontinuous ‘archipelagos’ about 1–10 nm in size. The choice of electrolytes can either facilitate or impede the coalescence of domains. The transformation microstructure gives rise to strain gradients, and their distribution is shown to alter the ion diffusivity in cathode NPs by a factor of ten or more. Our work demonstrates that understanding and controlling transformation microstructure in ion-insertion electrodes are critical for the development of rechargeable ion batteries^{36–38}, and potentially other electrochemical materials in fuel cells, desalination, separation and electrochromics³⁹.

We start with single-crystalline pristine $\lambda\text{-MnO}_2$ cathode NPs (81 ± 25 nm in diameter, Supplementary Fig. 1, Methods and Supplementary Note 1.2), which exhibit uniform intraparticle phase and strain distribution. Figure 1a illustrates the principle of phase orientation mapping. A small-convergence-angle electron nanobeam of 1.7 nm probe size is scanned in 2 nm steps across the NP to record a four-dimensional dataset of diffraction patterns (Supplementary Note 2 and Supplementary Table 1). Beam damage is negligible as revealed from the high-angle annular dark-field (HAADF) images and the analysis of diffracted beam intensity of the NP before and after a 4D-STEM scan

(Supplementary Fig. 2). The collected four-dimensional dataset allows for high-spatial-resolution mapping of phase orientations and precise measurement of lattice spacing and strain (Supplementary Fig. 3; estimated 0.9% for the upper bound of systematic strain errors among NPs, and precision within the same NP can be 0.3%, Supplementary Note 3). The orientation maps, derived from a data-mining approach, show a uniform spatial distribution of single-phase orientation in all the six pristine NPs we study ($[110]_c$ in Fig. 1b,c, more NPs in Supplementary Fig. 3, method in Supplementary Fig. 4). Similarly, the intraparticle strains (x , $[110]_c$; y , $[001]_c$) are spatially uniform ($<1\%$, Fig. 1d and Supplementary Fig. 3). The strain is measured as the percentage change in local lattice parameters of the NPs along the x and y directions in reference to the averaged lattice parameters of pristine NPs calibrated from XRD (Supplementary Note 3), which is also known as ‘Lagrange strain’⁴⁰.

The pristine $\lambda\text{-MnO}_2$ NPs then undergo galvanostatic charge and discharge in aqueous electrolyte (1 M $\text{Mg}(\text{NO}_3)_2$) at C/10 to allow Mg^{2+} insertion, during which the composition homogeneity is maintained. At the ensemble level, the continuous shift of XRD peaks of the cathode NPs from cubic to tetragonal spinel phase (Fig. 1e) during discharge suggests a solid-solution-type phase transition, which promotes composition homogeneity⁴¹. It is distinctive from the multiphase transition in micrometre-sized $\lambda\text{-MnO}_2$ particles associated with the separation of cubic and tetragonal spinel phases^{9,26}. On the single-particle level, monochromated EELS is performed at $\text{Mn}_{L_{2,3}}$ edges to map and visualize Mn oxidation state at 2 nm spatial resolution for pristine and discharged cathode NPs. The spectral analysis of Mn oxidation state (L_3/L_2 intensity ratio analysis, Supplementary Note 3.10)⁴² in pristine NPs confirms uniform distribution of Mn^{4+} (Fig. 1f, EELS spectra in Supplementary Fig. 5 and EELS mapping of three more NPs in Supplementary Fig. 6). The intermediate and fully discharged cathode NPs show reduced Mn oxidation states due to Mg^{2+} insertion, while maintaining uniform spatial distribution of electronic structures (Fig. 1f, EELS spectra in Fig. 1g and EELS mapping of six more NPs in Supplementary Fig. 6). Energy dispersive spectroscopy (EDS) maps of fully discharged NPs confirm uniform intraparticle distributions of Mg, Mn and O elements (Supplementary Fig. 7). The atomic-scale HAADF images further reveal the occupancy of tetrahedral sites by inserted Mg^{2+} and the formation of the tetragonal spinel structure (Supplementary Fig. 1). These findings collectively suggest that chemical composition homogeneity is achieved in our NP system, consistent with the high elastic strain energy penalty of phase separation in nanoscale cathode particles⁴³.

Despite the chemical composition homogeneity, the newly formed tetragonal spinel phase in the cathode NPs exhibits different crystallographic orientations, which are quantified and visualized at the nanoscale. As shown in Fig. 1h, a fully discharged cathode NP is oriented at the $[110]_c$ observation angle normal to the c axis of the MnO_6 octahedra, ideal for investigating the structural change driven by the Jahn–Teller effect. While the collocated EELS map confirms the uniform spatial distribution of reduced Mn oxidation state within the NP (Fig. 1i), the tetragonal spinel $[100]_t$ and $[111]_t$ phase orientations are found to coexist in the NP (Fig. 1j, Supplementary Fig. 8 and Supplementary Note 3.5). A pseudocubic spinel structure along its $[110]_c$ zone axis locates in the transition region between $[100]_t$ and $[111]_t$ domains (green region in Fig. 1j), owing to the large lattice difference (Supplementary Fig. 4). For clarification, we use ‘domains’ to describe structures of different crystallographic orientations of tetragonal phases hereinafter, following literature conventions^{8,10}. Note that the oriented phase domains have three-dimensional morphologies that can vary along the incident beam direction, which could introduce biases in quantitative analysis of domain microstructures using the two-dimensional (2D) projection data. The extent of these biases can be quantified by the sharpness of diffraction spots, which can be taken into consideration in our study of oriented phase domains and their formation mechanism (Supplementary Figs. 9–11 and Supplementary Note 4).

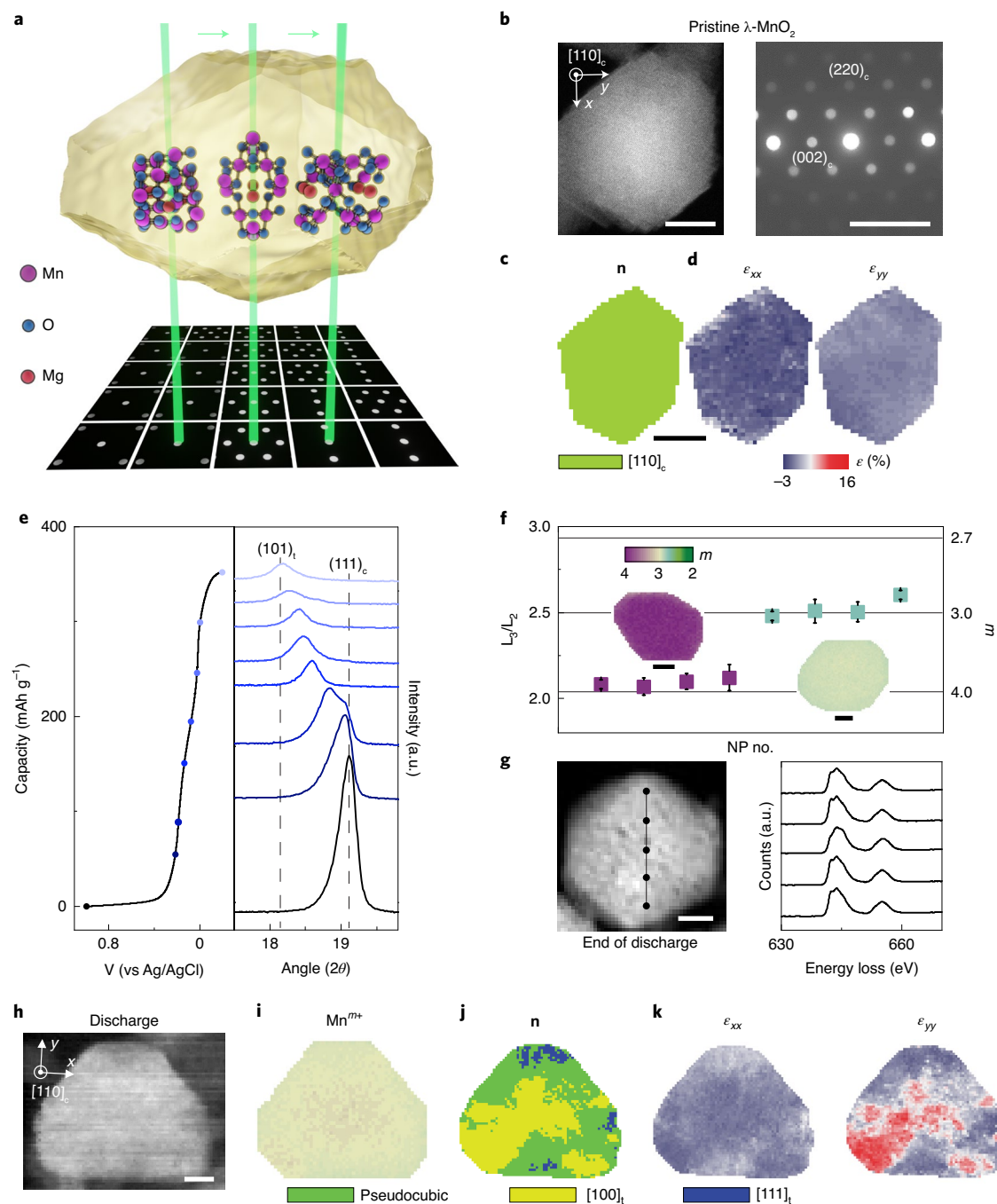


Fig. 1 | Oriented phase domains in compositionally uniform cathode NPs.

a, Schematic of 4D-STEM mapping of local lattice structure for cathode NPs. **b**, HAADF image of the pristine λ - MnO_2 cathode NP before discharge (left) and the corresponding summed 4D-STEM pattern (right) to show single crystallinity. Scale bars, 20 nm (left) and 5 nm^{-1} (right). **c, d**, Crystallographic orientation **n** (**c**) and strain distribution ϵ_{xx} and ϵ_{yy} (**d**) in the pristine MnO_2 cathode NP. Scale bar, 20 nm. **e**, The first galvanostatic discharge for the cathode NPs and the corresponding XRD patterns of the NPs at various cutoff voltages. A charge process was performed to remove residual cations before the discharge (Supplementary Fig. 1). a.u., arbitrary units. **f**, Averaged Mn L_3/L_2 ratio and the converted Mn oxidation state (m) for each NP calculated from EELS mapping: pristine NPs (purple) and NPs at the end of discharge (light green). Data are

presented as mean \pm s.d. on the basis of n pixels of L_3/L_2 ratio within each NP (n is 722, 935, 1,044, 626, 1,727, 1,190, 921 and 1,888 from left to right). Inset: representative EELS maps of Mn oxidation state for individual NPs (left, pristine; right, end of discharge). Scale bars, 20 nm. **g**, ADF image of a cathode NP at the end of discharge (left) and representative EELS spectra (right) of Mn $L_{2,3}$ edges collected at the black dotted locations across the NP labelled on the left, showing consistent line profiles. Scale bar, 20 nm. **h**, Virtual ADF image of a representative cathode NP at the end of discharge. Scale bar, 20 nm. **i–k**, Mn oxidation state map (**i**), crystallographic orientation map (**j**) and strain maps (**k**) for the same cathode NP as shown in **h**. The strain maps (**d, k**) and the maps of Mn oxidation states (**f, i**) share the same colour bars, respectively.

Non-uniform strain distribution is observed within the particle and spatially correlated with the distribution of domains (Fig. 1k), confirming that the structural distortion is created by the formation

of domains of different crystallographic orientations. Such spatial distribution of domains, that is, domain morphology, stays unchanged over one week after discharge (repeated 4D-STEM mapping in

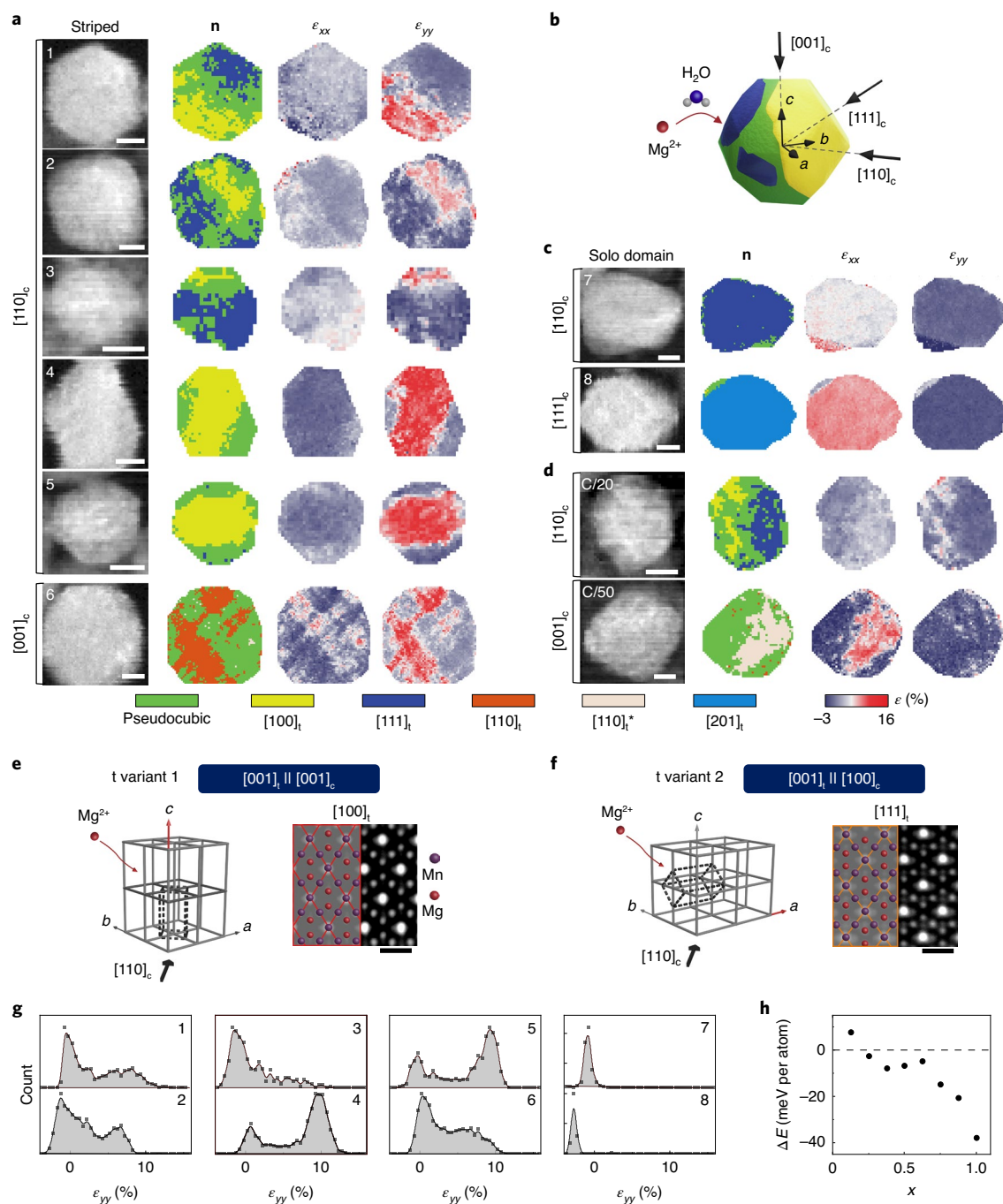


Fig. 2 | The oriented phase domain morphologies in discharged NPs and the origin from the symmetry change. a, c, Virtual ADF images, orientation maps and strain maps for the cathode NP at the end of discharge at C/10 in the aqueous electrolyte. The Miller indices corresponding to the cubic phase are used for describing the observation angle, as they remain unchanged during phase transformation (Supplementary Note 3.6). NPs are categorized on the basis of the oriented domain morphologies as striped (a) and solo domain (c). $[110]_t^*$ indicates $[110]_t$ orientation with 90° in-plane rotation. More NPs are characterized and shown in Supplementary Fig. 12. Scale bars, 20 nm. **b,** Schematic of a cathode NP composed of multiple oriented domains viewed from different crystallographic axes. **d,** Virtual ADF images, orientation maps

and strain maps for representative cathode NPs at the end of discharge at C/20 and C/50. Scale bars, 20 nm. **e, f,** The cubic structure viewed at $[110]_c$ can transform into tetragonal spinel structure either of $[100]_t$ orientation when the c axis is stretched (e) or of $[111]_t$ orientation when the a or b axis is stretched (f). Experimental HAADF images show the atomic structures of $[100]_t$ orientation (e) and $[111]_t$ orientation (f) in the cathode NPs at the end of discharge (right-hand panels). Scale bars, 0.5 nm. **g,** ϵ_{yy} histogram exhibiting distinctive profiles corresponding to the oriented phase domain morphologies categorized in a and c. **h,** Energy difference of the tetragonal phase relative to the cubic phase as a function of x in $\text{Mg}_x\text{Mn}_2\text{O}_4$ calculated from DFT.

Supplementary Fig. 12). The collocated EELS and 4D-STEM of the same NP (Fig. 1h–k) at matched spatial resolution show an intriguing spatial decoupling between chemical composition and crystallographic orientation in electrochemical ion insertion, suggesting the importance

of independently investigating the formation mechanism and impact of oriented phase domains.

The spatial distributions of oriented phase domains in the cathode NPs exhibit surprising complex morphologies. Major domains (with

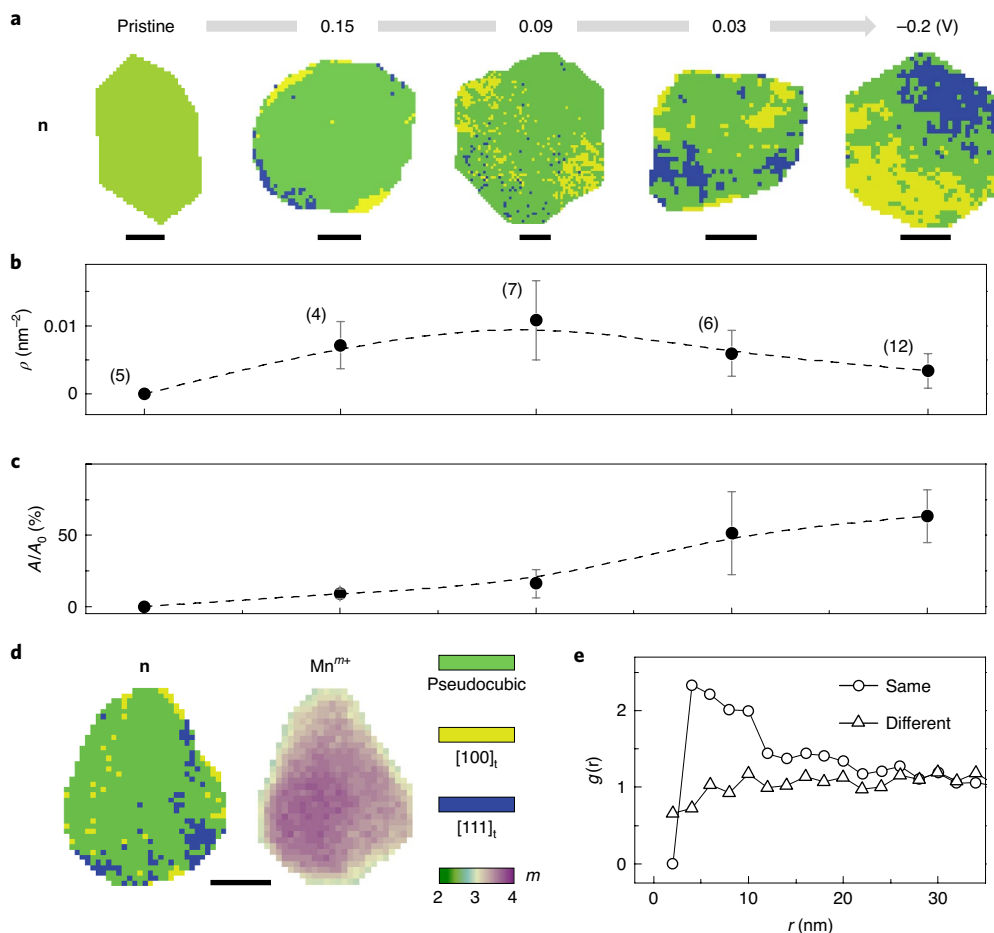


Fig. 3 | Nucleation, growth and coalescence of oriented phase domains within cathode NPs across the entire discharge process. **a**, The orientation maps of cathode NPs collected at five different cutoff voltages (V versus Ag/AgCl) in the first discharge in the aqueous electrolyte at C/10. More NPs analysed in Supplementary Fig. 19. Scale bars, 20 nm. **b,c**, ρ (**b**) and area fraction (A/A_0) (**c**) of projected domains statistically calculated from the multiple NPs at different

cutoff voltages. The number of NPs analysed is noted in brackets. Data are presented as mean \pm s.d. on the basis of 5, 4, 7, 6 and 12 cathode NPs at different cutoff voltages. **d**, Orientation map and EELS map of Mn oxidation state for a representative NP along the [110]_c zone axis at 0.09 V (versus Ag/AgCl). Scale bar, 20 nm. **e**, $g(r)$ for domains of the same orientation and different orientations averaged for six cathode NPs at 0.09 V (versus Ag/AgCl).

an effective radius of 20–50 nm) are observed in the 12 NPs checked at the end of discharge (Figs. 1j and 2a–c and Supplementary Fig. 12). The domains extend into the three-dimensional volume of NPs (Fig. 2b), as evidenced by the similar major domains at various observation angles of [110]_c, [001]_c and [111]_c (Fig. 2a,c). The ‘striped’ NPs contain one or several major domains (Figs. 1j and 2a) extending from one edge to the other. Other, ‘solo-domain’, NPs exhibit one major domain spanning the whole NP (Fig. 2c). The domain morphologies do not change over the NP size range of 40–100 nm. These oriented phase domains persist in NPs discharged at much lower current rates of C/20 and C/50 (Fig. 2d), suggesting that the domains are stable.

Due to the fcc symmetry of cubic spinel, *a*, *b* and *c* axes are equally likely to be stretched as the lattice symmetry lowers during phase transformation, causing the coexistence of crystallographically equivalent orientation variants. For example, the cubic spinel structure observed along its [110]_c zone axis can transform to either [100]_t or [111]_t as the *c* axis or *a/b* axis is strained (configurations resolved in Fig. 2e,f from differences in the atomic distance), respectively, which is consistently observed in ten NPs (Figs. 1j and 2a,c and Supplementary Fig. 12) and matches the group–subgroup relationship⁸. The NP observed along the [001]_c direction contains [110]_t variants with 90° in-plane rotations (Fig. 2a, NP 6), matching the straining of the *a* and *b* axes of the cubic spinel structure (Supplementary Fig. 13). As the orientation variants are stretched in different directions, they present

distinctive strains in the zone planes, for example, $\epsilon_{xx} = 0\%$, $\epsilon_{yy} = 15\%$ for [100]_t and $\epsilon_{xx} = 7\%$, $\epsilon_{yy} = 0\%$ for [111]_t (Supplementary Fig. 4). The spatial distribution of strains is therefore dependent on the domain morphologies (Fig. 2a,c). The histogram of ϵ_{yy} exhibits a continuous distribution of multiplex profiles for the striped morphologies, and a sharp, single-peak profile for solo-domain morphology with high strain uniformity (Fig. 2g). The strain within each domain can have slight variations, which we attribute to the presence of local structural disorder from evidence obtained using geometric phase analysis⁴⁴ and cepstral analysis⁴⁵ (Supplementary Figs. 14–18 and Supplementary Table 2). The formation of distinct domains, as well as structural disorder, allows for relaxation of the internal strain distributions to some extent (Supplementary Note 4.7).

Density functional theory (DFT) calculations show that the energy difference between Mg_xMn₂O₄ in tetragonal symmetry and cubic symmetry increases as *x* increases, where the tetragonal symmetry has the lower energy (Fig. 2h and Supplementary Note 4.1), providing the driving force for the phase transformation. This is consistent with the solo-domain NPs (Fig. 2c), where a single tetragonal domain spans the whole NP at the end of discharge. However, the other NPs appear not fully transformed into the tetragonal symmetry, indicating the presence of kinetic barriers in the phase transformation. Furthermore, we note that while the tetragonal symmetry becomes more energetically favourable as *x* increases the energy difference is comparable to $k_B T$,

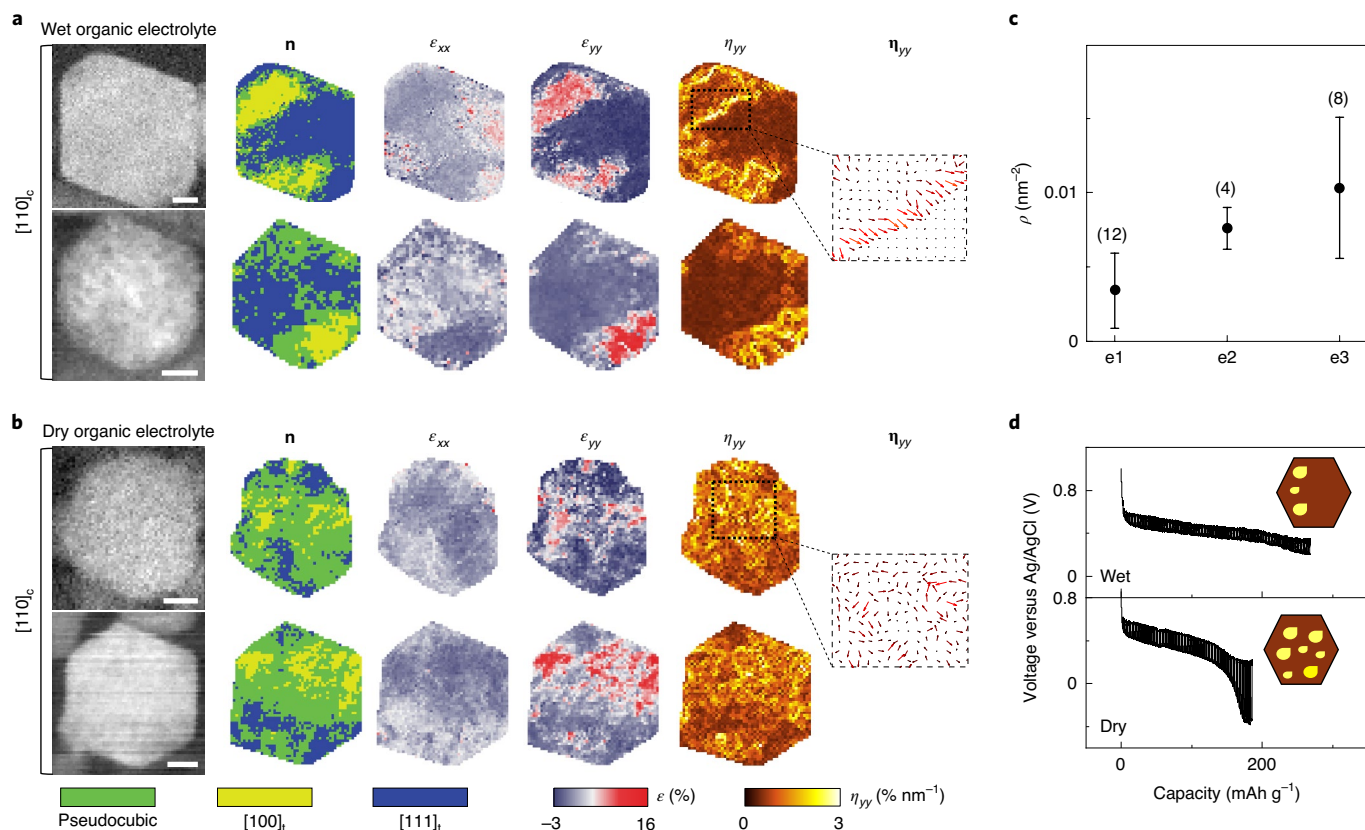


Fig. 4 | Oriented phase domains in different electrolyte conditions and their impacts on strain gradients and ion diffusion. **a, b**, Virtual ADF images, orientation maps, strain maps and strain gradient maps of ϵ_{yy} (η_{yy}) for four representative cathode NPs after discharge in the wet organic electrolyte (**a**) and the dry organic electrolyte (**b**). Zoomed-in images show the strain gradient vectors of ϵ_{yy} (η_{yy}). Twelve NPs are analysed in total (more NPs shown in Supplementary Fig. 27). Scale bars, 20 nm. **c**, The average number density of 2D

projected domains for cathode NPs in different electrolyte conditions. ‘e1’, ‘e2’ and ‘e3’ stand for aqueous electrolyte, wet organic electrolyte and dry organic electrolyte, respectively. The number of analysed NPs is noted in brackets. Data are presented as mean \pm s.d. on the basis of 12, 4 and 8 cathode NPs in different electrolytes. **d**, The voltage responses of the cathode NPs in GITT measurements during the first discharge in the wet and dry organic electrolytes. Schematics indicating the distributions of strain gradients are given in the insets.

consistent with the coexistence of phases, some with variable orientations and strain.

To further understand and quantitatively describe the formation mechanism of oriented phase domains, we map cathode NPs collected at five different cutoff voltages during discharge, which elucidate a nucleation, growth and coalescence process. At the initial stage of discharge (0.15 V (versus Ag/AgCl)), small domains of orientation variants are observed to first nucleate near the NP surface (Fig. 3a, consistent among more NPs in Supplementary Fig. 19). In the middle of discharge (0.09 V (versus Ag/AgCl)), more domains start to form, including the ones in the bulk. The number density of the 2D projected domains, ρ , increases to a maximum ($0.011 \pm 0.006 \text{ nm}^{-2}$, Fig. 3b), with a growing domain area percentage ($16\% \pm 10\%$, Fig. 3c). The spatial distribution of the electronic structure in the NPs remains largely uniform, as shown by the EELS map of a representative NP in Fig. 3d (more EELS maps of NPs in Supplementary Fig. 6). As the discharge continues (0.03 V (versus Ag/AgCl)), ρ starts to decrease (Fig. 3b) while the domain area percentage keeps increasing (Fig. 3c). This decrease indicates the coalescence of domains that lasts until the end of discharge. The domain evolution mechanism is fundamentally different from the well-known diffusion- and reaction-limited transformation mechanisms, such as the ‘shrinking-core’ behaviour, where the phase boundary moves inwards from all active surfaces of the particle, or the ‘intercalation wave’ mechanism, where a single (or a small number of) phase front(s) propagates across the whole particle¹⁰. In our system, the oriented phase domains undergo nucleation at multiple locations across NPs

from the solid-solution parent phase, and then grow and coalesce, leading to the complex domain morphology at the end of discharge (Fig. 2a–d). Upon further charge, the domain morphology partly disappears as the tetragonal spinel changes back to the cubic spinel in cathode NPs (Supplementary Fig. 19). An approximation based on the non-binary fraction analysis of three-dimensional oriented phase domains also supports the domain formation mechanism obtained from 2D analysis (Supplementary Fig. 20 and Supplementary Note 5).

The growth of the oriented domains appears to be self-arrested. For NPs that exhibit the morphology of a pseudocubic phase sandwiched between tetragonal domains (for example, Fig. 3a, at -0.2 V (versus Ag/AgCl)), the self-arrest can be attributed to an unfavourable increase in interface misfit strain should the domains continue to grow and come in contact with each other. In the case of epitaxially aligned interfaces, results from DFT calculations suggest that the presence of a cubic phase in between tetragonal domains of varying orientation can lead to lower interface lattice mismatch than if the domains are directly in contact with each other (Supplementary Figs. 21 and 22). This self-arresting phase transformation is reminiscent of those studied in the martensitic transformation of shape memory alloys⁴. During martensitic transformation, distinct symmetry-equivalent variants of the martensite phase first nucleate locally in different regions of the material. As the variants grow, they eventually present mutual obstacles for continued growth and the transformation becomes self-arresting, until further driving force is provided for certain variants to grow at the expense of others.

The oriented phase domains in the cathode NPs are spatially correlated with a characteristic projected correlation length of approximately 15 nm (Supplementary Note 5.3). The radial distribution functions ($g(r)$) for domains of the same and different types of variant are calculated for cathode NPs at various cutoff voltages (Supplementary Note 5), where r is the interdomain centre-of-mass distance. The probability of finding domains of the same variant is higher than that of finding domains of different variants when the interdomain distance is smaller than 15 nm, which is consistently observed at different cutoff voltages (Fig. 3e and Supplementary Fig. 20). The spatial correlation points to the existence of elastic interactions between domains that favour the formation of domains of the same orientation nearby, reminiscent of the coherency strain that suppresses chemical phase separation^{34,46}. As a result, domain coalescence is facilitated. Protrusion structures in connection of two domains of the same orientation are observed in cathode NPs (for example NPs 3 and 6 in Fig. 2a), with the characteristic neck formation at the onset of coalescence driven by surface energy minimization⁴⁷.

Next, we extend our study to domain morphologies in different electrolytes. Our cathode NPs undergo galvanostatic charge and discharge at C/10 in wet organic electrolyte (0.5 M Mg(ClO₄)₂, 0.6 M water in acetonitrile) and dry organic electrolyte (0.5 M Mg(ClO₄)₂ in acetonitrile), respectively (Supplementary Figs. 23 and 24 and Supplementary Note 6). In both electrolytes, XRD shows that solid-solution-type phase transitions are achieved (Supplementary Fig. 23). EELS and EDS mapping confirm the reduction of Mn oxidation state due to Mg²⁺ insertion and uniform intraparticle composition at the end of discharge (Supplementary Figs. 25 and 26 and Supplementary Table 3). In the wet organic electrolyte, fully discharged cathode NPs exhibit major island-like domains (Fig. 4a, two more NPs in Supplementary Fig. 27) similar to those in the aqueous electrolyte. The strain uniformity, quantified as the strain gradient (Fig. 4a), is minimized within the major domains (0.5% nm⁻¹ as calculated from the 4D-STEM datasets), with the high strain gradient (2–3% nm⁻¹) locating at the domain boundaries. In contrast, in the dry organic electrolyte, small (1–10 nm) and scattered domains are observed (Fig. 4b, six more NPs in Supplementary Fig. 27, domain formation and development in Supplementary Fig. 28). The discharged cathode NPs adopt an archipelago-like morphology and have a higher ρ than those discharged in the wet organic and aqueous electrolytes (Fig. 4c). High strain gradients (2–3% nm⁻¹) are observed across cathode NPs with irregularly distributed directions (Fig. 4b, Supplementary Figs. 29 and 30 and Supplementary Note 6).

Domain morphologies can impact Mg²⁺ diffusion in the cathode NPs. The galvanostatic intermittent titration technique (GITT) is used to evaluate the ion diffusion for different domain morphologies (Fig. 4d). In GITT, the instant voltage jump after applying current is attributed to the uncompensated resistance and charge transfer resistance, while the gradual voltage change in the latter period of the current pulse in synchronization with the concentration overpotential is due to the solid-state diffusion^{48,49}. The diffusion coefficient, D_s , is related to the gradual voltage (V) change over time t as $D_s \propto (dV/d\sqrt{t})^{-2}$, where the current pulse duration is constant⁴⁹. In the wet organic electrolyte, the gradual voltage change remains approximately 0.1 V during the whole discharge process. In contrast, in the dry organic electrolyte, the gradual voltage change increases substantially from 0.16 V to 0.57 V at the end of the plateau, suggesting slower ion diffusion by a factor of 18 (Supplementary Note 7). Considering the intraparticle chemical composition homogeneity and the unlikelihood of solvent co-insertion, we associate the change in diffusion with the structural distortions and high strain gradients created by archipelago-like domain morphology (Supplementary Note 7). The high strain gradients across the NPs in the dry organic electrolyte are associated with semicoherent interfaces and stacking faults (Supplementary Fig. 27) that can disturb the ion diffusion pathways²¹.

In conclusion, our results show that oriented phase domains and associated strain gradients can emerge and persist in cathode materials during ion intercalation and the associated phase transition over a wide range of current rates and in different electrolytes. The observed large change in ion diffusivity and electrochemical performance can be correlated with the heterogeneous distribution of oriented phase domains and strain gradients across the domain boundaries. These results offer fundamental insights into the microstructural development originating from symmetry changes, beyond the conventional understanding of inhomogeneity resulting from diffusion- and reaction-limited mechanisms¹⁰. Broadly speaking, our approach, combining collocated chemical phase, phase orientation and strain gradient mapping with ensemble electrochemical tests, is highly applicable to other phase-transforming electrode systems, particularly those that undergo large lattice distortions^{13,36}. Our findings project nanoscale microstructure engineering toward mitigating chemomechanical degradations and achieving the reliable operation of high-capacity electrode materials.

Online content

Any methods, additional references, Nature Research reporting summaries, source data, extended data, supplementary information, acknowledgements, peer review information; details of author contributions and competing interests; and statements of data and code availability are available at <https://doi.org/10.1038/s41563-022-01381-4>.

References

1. Stupp, S. I. & Braun, P. V. Molecular manipulation of microstructures: biomaterials, ceramics, and semiconductors. *Science* **277**, 1242–1248 (1997).
2. Dahmen, U. in *Encyclopedia of Physical Science and Technology* (ed. Meyers, R. A.) 821–853 (Elsevier, 2003).
3. Xu, Z. et al. Charge distribution guided by grain crystallographic orientations in polycrystalline battery materials. *Nat. Commun.* **11**, 83 (2020).
4. Gerstein, G., L'vov, V. A., Zak, A., Dudzinski, W. & Maier, H. J. Direct observation of nano-dimensional internal structure of ferromagnetic domains in the ferromagnetic shape memory alloy Co–Ni–Ga. *J. Magn. Magn. Mater.* **466**, 125–129 (2018).
5. Katayama, K. et al. Orientation control and domain structure analysis of {100}-oriented epitaxial ferroelectric orthorhombic HfO₂-based thin films. *J. Appl. Phys.* **119**, 134101 (2016).
6. Sun, L. G., He, X. Q. & Lu, J. Nanotwinned and hierarchical nanotwinned metals: a review of experimental, computational and theoretical efforts. *npj Comput. Mater.* **4**, 6 (2018).
7. Thackeray, M. M. & Amine, K. LiMn₂O₄ spinel and substituted cathodes. *Nat. Energy* **6**, 566–566 (2021).
8. Chiang, Y. M., Wang, H. F. & Jang, Y. I. Electrochemically induced cation disorder and phase transformations in lithium intercalation oxides. *Chem. Mater.* **13**, 53–63 (2001).
9. Kim, C. et al. Direct observation of reversible magnesium ion intercalation into a spinel oxide host. *Adv. Mater.* **27**, 3377–3384 (2015).
10. Merryweather, A. J., Schnedermann, C., Jacquet, Q., Grey, C. P. & Rao, A. Operando optical tracking of single-particle ion dynamics in batteries. *Nature* **594**, 522–528 (2021).
11. Peres, J. P., Weill, F. & Delmas, C. Lithium/vacancy ordering in the monoclinic Li_xNiO₂ (0.50 ≤ x ≤ 0.75) solid solution. *Solid State Ion.* **116**, 19–27 (1999).
12. Shao-Horn, Y., Levasseur, S., Weill, F. & Delmas, C. Probing lithium and vacancy ordering in O3 layered Li_xCoO₂ (x ≈ 0.5): an electron diffraction study. *J. Electrochem. Soc.* **150**, A366 (2003).
13. Berthelot, R., Carlier, D. & Delmas, C. Electrochemical investigation of the P2–Na_xCoO₂ phase diagram. *Nat. Mater.* **10**, 74–80 (2011).

14. Ben Yahia, H., Shikano, M. & Kobayashi, H. Phase transition mechanisms in Li_xCoO_2 ($0.25 \leq x \leq 1$) based on group-subgroup transformations. *Chem. Mater.* **25**, 3687–3701 (2013).
15. Gu, M. et al. Formation of the spinel phase in the layered composite cathode used in Li-ion batteries. *ACS Nano* **7**, 760–767 (2013).
16. Shukla, A. K. et al. Unravelling structural ambiguities in lithium- and manganese-rich transition metal oxides. *Nat. Commun.* **6**, 8711 (2015).
17. Jarvis, K. A. et al. Formation and effect of orientation domains in layered oxide cathodes of lithium-ion batteries. *Acta Mater.* **108**, 264–270 (2016).
18. Shukla, A. K. et al. Effect of composition on the structure of lithium- and manganese-rich transition metal oxides. *Energy Environ. Sci.* **11**, 830–840 (2018).
19. Shao-Horn, Y. et al. Lithium and vacancy ordering in $\text{T}^2\text{-Li}_x\text{CoO}_2$ derived from O_2 -type LiCoO_2 . *Chem. Mater.* **15**, 2977–2983 (2003).
20. Kuhne, M. et al. Reversible superdense ordering of lithium between two graphene sheets. *Nature* **564**, 234–239 (2018).
21. Sun, H. B. et al. Tailoring disordered/ordered phases to revisit the degradation mechanism of high-voltage $\text{LiNi}_{0.5}\text{Mn}_{1.5}\text{O}_4$ spinel cathode materials. *Adv. Funct. Mater.* **32**, 2112279 (2022).
22. Lim, J. et al. Origin and hysteresis of lithium compositional spatiodynamics within battery primary particles. *Science* **353**, 566–571 (2016).
23. Deng, H. D. et al. Correlative image learning of chemo-mechanics in phase-transforming solids. *Nat. Mater.* **21**, 547–554 (2022).
24. Ulvestad, A. et al. Topological defect dynamics in operando battery nanoparticles. *Science* **348**, 1344–1347 (2015).
25. Han, S. Y. et al. Stress evolution during cycling of alloy-anode solid-state batteries. *Joule* **5**, 2450–2465 (2021).
26. Chen, W. et al. Effects of particle size on Mg^{2+} ion intercalation into $\lambda\text{-MnO}_2$ cathode materials. *Nano Lett.* **19**, 4712–4720 (2019).
27. Canepa, P. et al. Odyssey of multivalent cathode materials: open questions and future challenges. *Chem. Rev.* **117**, 4287–4341 (2017).
28. Lin, F. et al. Synchrotron X-ray analytical techniques for studying materials electrochemistry in rechargeable batteries. *Chem. Rev.* **117**, 13123–13186 (2017).
29. Lewis, J. A. et al. Linking void and interphase evolution to electrochemistry in solid-state batteries using operando X-ray tomography. *Nat. Mater.* **20**, 503–510 (2021).
30. Yin, Z. W. et al. Advanced electron energy loss spectroscopy for battery studies. *Adv. Funct. Mater.* **32**, 2107190 (2021).
31. Ophus, C. Four-dimensional scanning transmission electron microscopy (4D-STEM): from scanning nanodiffraction to ptychography and beyond. *Microsc. Microanal.* **25**, 563–582 (2019).
32. Liu, X. et al. Local electronic structure variation resulting in Li ‘filament’ formation within solid electrolytes. *Nat. Mater.* **20**, 1485–1490 (2021).
33. Park, J. et al. Fictitious phase separation in Li layered oxides driven by electro-autocatalysis. *Nat. Mater.* **20**, 991–999 (2021).
34. Cogswell, D. A. & Bazant, M. Z. Coherency strain and the kinetics of phase separation in LiFePO_4 nanoparticles. *ACS Nano* **6**, 2215–2225 (2012).
35. Gibot, P. et al. Room-temperature single-phase Li insertion/extraction in nanoscale Li_xFePO_4 . *Nat. Mater.* **7**, 741–747 (2008).
36. Liang, Y., Dong, H., Aurbach, D. & Yao, Y. Current status and future directions of multivalent metal-ion batteries. *Nat. Energy* **5**, 646–656 (2020).
37. Hou, S. et al. Solvation sheath reorganization enables divalent metal batteries with fast interfacial charge transfer kinetics. *Science* **374**, 172–178 (2021).
38. Lu, J., Chen, Z., Pan, F., Cui, Y. & Amine, K. High-performance anode materials for rechargeable lithium-ion batteries. *Electrochem. Energy Rev.* **1**, 35–53 (2018).
39. Sood, A. et al. Electrochemical ion insertion from the atomic to the device scale. *Nat. Rev. Mater.* **6**, 847–867 (2021).
40. Padgett, E. et al. The exit-wave power-cepstrum transform for scanning nanobeam electron diffraction: robust strain mapping at subnanometer resolution and subpicometer precision. *Ultramicroscopy* **214**, 112994 (2020).
41. Malik, R., Zhou, F. & Ceder, G. Kinetics of non-equilibrium lithium incorporation in LiFePO_4 . *Nat. Mater.* **10**, 587–590 (2011).
42. Laffont, L. & Gibot, P. High resolution electron energy loss spectroscopy of manganese oxides: application to Mn_3O_4 nanoparticles. *Mater. Charact.* **61**, 1268–1273 (2010).
43. Li, J. et al. Size-dependent kinetics during non-equilibrium lithiation of nano-sized zinc ferrite. *Nat. Commun.* **10**, 93 (2019).
44. Rouviere, J. L. & Sarigiannidou, E. Theoretical discussions on the geometrical phase analysis. *Ultramicroscopy* **106**, 1–17 (2005).
45. Shao, Y. T. et al. Cepstral scanning transmission electron microscopy imaging of severe lattice distortions. *Ultramicroscopy* **231**, 113252 (2021).
46. Ulvestad, A. et al. Single particle nanomechanics in operando batteries via lensless strain mapping. *Nano Lett.* **14**, 5123–5127 (2014).
47. Jin, B., Sushko, M. L., Liu, Z., Jin, C. & Tang, R. In situ liquid cell TEM reveals bridge-induced contact and fusion of Au nanocrystals in aqueous solution. *Nano Lett.* **18**, 6551–6556 (2018).
48. Sun, W. et al. Zn/ MnO_2 battery chemistry with H^+ and Zn^{2+} coininsertion. *J. Am. Chem. Soc.* **139**, 9775–9778 (2017).
49. Verma, A. et al. Galvanostatic intermittent titration and performance based analysis of $\text{LiNi}_{0.5}\text{Co}_{0.2}\text{Mn}_{0.3}\text{O}_2$ cathode. *J. Electrochem. Soc.* **164**, A3380–A3392 (2017).

Publisher’s note Springer Nature remains neutral with regard to jurisdictional claims in published maps and institutional affiliations.

Springer Nature or its licensor holds exclusive rights to this article under a publishing agreement with the author(s) or other rightsholder(s); author self-archiving of the accepted manuscript version of this article is solely governed by the terms of such publishing agreement and applicable law.

© The Author(s), under exclusive licence to Springer Nature Limited 2022

¹Department of Materials Science and Engineering, University of Illinois, Urbana, IL, USA. ²Materials Research Laboratory, University of Illinois, Urbana, IL, USA. ³Department of Mechanical Science and Engineering, University of Illinois, Urbana, IL, USA. ⁴Department of Chemical and Biomolecular Engineering, University of Illinois, Urbana, IL, USA. ⁵Department of Chemistry, University of Illinois, Urbana, IL, USA. ⁶Joint Center for Energy Storage Research, Argonne National Laboratory, Lemont, IL, USA. ⁷Shell International Exploration and Production Inc., Houston, TX, USA. ⁸Beckman Institute for Advanced Science and Technology, University of Illinois, Urbana, IL, USA. ✉ e-mail: jianzuo@illinois.edu; qchen20@illinois.edu

Methods

Sample preparation

Spinel λ - MnO_2 particles were prepared by acid leaching of the as-purchased LiMn_2O_4 particles (Sigma-Aldrich) following the literature method²⁶. LiMn_2O_4 particles (2 g) were soaked in 200 ml 0.1 M HCl aqueous solution (Alfa Aesar) and stirred at 300 r.p.m. overnight to produce delithiated $\text{Li}_x\text{Mn}_2\text{O}_4$ particles. The λ - MnO_2 particles obtained after acid leaching are polydisperse in size²⁶. The monodispersed, single-crystalline λ - MnO_2 NPs were selected via dispersion and centrifugation as detailed in Supplementary Note 1.2. Working electrodes were prepared by mixing the NPs with carbon black (Alfa Aesar) and polyvinylidene fluoride (MTI Corporation) at a fixed mass ratio of 8:1:1 using 1-methyl-2-pyrrolidinone (Sigma-Aldrich) as the solvent. The mixture was ground in an Ar glovebox (MBRAUN, $\text{O}_2 < 0.1$ ppm and $\text{H}_2\text{O} < 0.1$ ppm) and cast on a stainless steel shim (Trinity Brand Industry) at a mass load of -1.0 to 1.5 mg cm^{-2} . The shim was then kept in vacuum (-85 kPa) at room temperature overnight to dry. The preparations of reference electrodes, counter electrodes, aqueous electrolytes, wet organic electrolytes and dry organic electrolytes are detailed in Supplementary Note 1.2.

Electrochemical characterizations

Electrochemical tests performed in this work include galvanostatic charge and discharge, GITT, cyclic voltammetry and electrochemical impedance spectroscopy (EIS), which were conducted in three-electrode beaker cells. In all the experiments (except cyclic voltammetry), a charge process was performed initially to remove the residual Li^+ ions from the cathode NPs. Galvanostatic charge and discharge were conducted in the voltage range of 1 V to -0.2 V (versus Ag/AgCl) for the aqueous and wet organic electrolytes and in the equivalent voltage range of 0.79 V to -0.41 V (versus Ag/Ag⁺) for the dry organic electrolyte, considering the difference in the potential of the reference electrodes (Supplementary Note 1.2). The current rate was set at $C/10$ (27 mA g^{-1} ; C means the current rate to fully charge or discharge the electrode in 1 h) and was varied. GITT was performed at a constant current rate of $C/20$ with 10 min discharge, followed by 1 h relaxation of voltage at the open-circuit stand to the steady state. About 200 pulses were performed during the first discharge. The cyclic voltammetry experiments were conducted in the voltage range of -0.4 V to 1.1 V (versus Ag/Ag⁺) in the dry organic electrolyte system at scan rates of 0.5 mV s^{-1} , 1 mV s^{-1} , 3 mV s^{-1} and 5 mV s^{-1} in sequence. EIS was performed in the frequency range from 200 kHz to 0.01 Hz with 10 mV perturbation using λ - MnO_2 NPs as the counter-electrode.

Structural and chemical characterizations

To prepare samples for the 4D-STEM, the cathode NPs were gently scratched off from the electrodes using a pair of clean stainless steel tweezers. The scratched materials were gently ground in a clean agate mortar for 3 min for dispersion with deionized water for the aqueous electrolyte or with acetonitrile for the wet and dry organic electrolytes. The dispersion was then drop-casted on a transmission electron microscopy grid (CF400-Cu, Electron Microscopy Sciences).

Electron microscopy including 4D-STEM, EELS mapping, HAADF imaging and EDS was conducted on a Themis Z (S)TEM (Thermo Fisher Scientific) operated at 300 kV. The microscope is equipped with a probe aberration corrector for aberration-corrected STEM. The 4D-STEM was performed at a convergence semi-angle of 0.64 mrad (calculated from the diffraction disk, corresponding to a 1.7 nm full-width at half-maximum probe size) using a 50 μm condenser (C2) and a camera length of 185 mm. The samples of NPs were tilted using a standard double-tilt holder so that the desired crystallographic axis of the spinel structure ($[110]_c$, $[001]_c$ or $[111]_c$) was nearly parallel to the incident electron beam. The electron probe was raster-scanned across the NPs using a step size of 2 nm and a diffraction pattern recorded at each probe position with a complementary metal-oxide-semiconductor

camera (Ceta Camera, Thermo Fisher Scientific). The dwell time is 0.1–0.2 s for each step. The beam current is 17 pA. The settings give an electron dose of about $2.7 \times 10^4 e^- \text{Å}^{-2}$ normalized by scan area. The semi-angle range used to generate the virtual ADF images is 1.5–21.9 mrad. Low-magnification HAADF imaging was performed in the 4D-STEM mode. The typical scan area is about 400 nm \times 400 nm. The dwell time is 2 μs and the size is 4,096 \times 4,096 pixels. The collection angle of the HAADF detector is 62–200 mrad. It gives an electron dose of about $2.2 \times 10^2 e^- \text{Å}^{-2}$.

The atomic-scale HAADF imaging was performed in normal STEM mode with a convergence angle of 18 mrad and a camera length of 115 mm. The beam current is 20–30 pA. The typical scan area is 17.9 nm \times 17.9 nm. The dwell time is 4 μs and the size is 2,048 \times 2,048 pixels. This gives an electron dose of about $8.2 \times 10^4 e^- \text{Å}^{-2}$. The process methods for atomic-scale HAADF images are detailed in Supplementary Note 3.11.

EELS spectrum imaging data were acquired in STEM mode with monochromator tuning to optimize the energy resolution. The convergence angle is 20 mrad. EELS signatures were recorded using a Gatan Imaging Filter CCD (charge-coupled device) using a 2.5 mm aperture and an energy dispersion of 0.1 eV per channel. The full-width at half-maximum of the zero-loss peak in vacuum was about 0.4 eV. For data acquisition, the beam current for signal collection was set to -60 – 100 pA and the camera length was 29.5 mm. Dual EELS data were acquired in signal-to-noise ratio mode with low-loss data acquisition set to 0 eV with exposure time of 0.0001 s and high-loss acquisition set to 520 eV with exposure time of 0.2 s. The electron probe was raster-scanned across the NPs using a step size of 2 nm for the EELS map with similar sampling points to those for 4D-STEM. For spectrum imaging, the pixel acquisition time was set to 0.2 s with three passes to improve signal quality. This gives an electron dose of about $5.6 \times 10^5 e^- \text{Å}^{-2}$. For the ADF image collected in the EELS mode, the dwell time is 1–8 μs and the size is 2,048 \times 2,048 pixels. The ADF image dimensions are about 95 nm \times 95 nm. This gives an electron dose of about $7.0 \times 10^3 e^- \text{Å}^{-2}$.

EDS mapping was performed using a continuous scan with a frame time of approximately 1 s and summed over about 1,000 frames. The total acquisition time was about 30 min. The beam current is 100–200 pA. The convergence angle is 18 mrad. Considering the scan area of the EDS maps (for example 140 nm \times 140 nm in Supplementary Fig. 7), this gives an electron dose of about $8.6 \times 10^5 e^- \text{Å}^{-2}$. For the HAADF image collected together with EDS mapping, the dwell time is 3.5 μs and the size is 2,048 \times 2,048 pixels. For each frame, this gives an electron dose of about $7.0 \times 10^3 e^- \text{Å}^{-2}$.

Sample drift during 4D-STEM, EELS and EDS data acquisition was automatically corrected using the STEM images of the NP acquired about every 50 4D-STEM patterns (or EELS pixels, or EDS frames) using the HAADF detector.

Scanning electron microscopy imaging of the samples was conducted on a Hitachi S4800 SEM at 10 kV and 5 μA . XRD (Bruker D8 Advance) characterization was conducted at a wavelength of 0.15406 nm with a scan rate of 1 s per step and a minimum interval of 0.01° (2θ).

Simulation of electron diffraction patterns

The theoretical diffraction patterns of various orientations for cubic spinel structure (λ - MnO_2 , $[110]_c$, $[001]_c$, $[111]_c$) and tetragonal spinel structure (MgMn_2O_4 , $[100]_t$, $[111]_t$, $[110]_t$, $[201]_t$, $[001]_t$, $[101]_t$) (Supplementary Fig. 4) were calculated using dynamic diffraction simulation with the Bloch wave method⁵⁰. The Bloch simulation was carried out on the basis of the approximation of an ionic model for atomic scattering. The simulated sample thickness was set to be 20 nm. The electron beam in the simulation was set up to mimic the experimental conditions. The results were displayed in the logarithmic scale to enhance the visibility of low-intensity diffraction peaks.

Analysis methods for 4D-STEM and EELS data

Local information on the lattice, including the phase, phase orientation and insertion-induced strain, in the cubic-to-tetragonal phase transformation was obtained and verified on the basis of our developed analysis methods detailed in Supplementary Note 3. The analysis software package imToolBox is available at <https://github.com/flysteven/imToolBox>. The procedures to obtain local information on the Mn oxidation state are detailed in Supplementary Note 3.10. Radial distribution function analysis is detailed in Supplementary Note 5.

DFT modelling

Procedures for the DFT modelling and analysis are detailed in Supplementary Note 4.

Data availability

The 4D-STEM and EELS data associated with this paper can be found at https://doi.org/10.13012/B2IDB-4717991_V1. Additional data are available on request from the corresponding authors.

Code availability

The codes used for the 4D-STEM strain mapping, oriented phase domain analysis, EELS analysis, radial distribution function and pair correlation function calculations can be accessed at <https://github.com/chenlabUIUC/OrientedPhaseDomain>. Additional codes are available on request from the corresponding authors.

References

50. Spence, J. C. H. & Zuo, J.-M. *Electron Microdiffraction* (Springer, 1992).

Acknowledgements

This work was primarily (sample preparation, majority of the 4D-STEM, EELS, XRD characterizations, electrochemical testing and data analysis) supported by the US Department of Energy, Office of Basic Energy Sciences, Division of Materials Sciences and Engineering, under award DE-SC0022035 (W.C., Z.T. and Q.C.). Some of the 4D-STEM experiments and the atomic-scale imaging were supported by Intel Corporation through an SRC project, award 54071821 (R.Y. and J.-M.Z.) and the Energy & Biosciences Institute through the EBI-Shell programme (W.C., S.P., C.Z., H.Y., J.-M.Z. and Q.C.). The DFT calculation and GITT and EIS measurements were supported in part by the US Army Construction Engineering Research Laboratory, Temperature Insensitive High-Density Lithium-Ion Batteries, award W9132T-21-2-0008 (A.X.B.Y., H.J., E.E., A.P. and P.V.B.). The preparation of dry solvents in the glovebox was supported in part by the Joint Center for Energy Storage Research (JCESR), an Energy Innovation

Hub funded by the US Department of Energy, Office of Science, Basic Energy Sciences (K.T. and A.A.G.). The analysis of XRD data by Rietveld refinement was supported by a DIGI-MAT fellowship from the NSF DGE programme, award 1922758 (Z.W.R. and D.P.S.) using instrumentation partially supported by NSF through the University of Illinois Materials Research Science and Engineering Center DMR-172063. We thank Z. Ou and J. W. Smith at the University of Illinois for discussions on radial distribution function. We thank C. Qian and L. Yao at the University of Illinois for assistance with MATLAB coding in the analysis of the radial distribution functions and strain gradients. We thank N. Admal at the University of Illinois for discussions on domain morphology and phase separation. We thank Y. Yang at Columbia University for discussions on electrochemical tests.

Author contributions

W.C., J.-M.Z. and Q.C. planned the research and led the project. W.C. performed material processing and conducted electrochemical measurements. X.Z., R.Y., W.C., S.P. and K.Y. conducted the 4D-STEM and STEM imaging. S.P., W.C., X.Z. and K.Y. conducted EELS mapping. W.C., X.Z., R.Y., J.-M.Z. and Q.C. analysed and interpreted the electron microscopy data. W.C., with assistance from H.A. and A.P., analysed and interpreted the electrochemical results. Z.W.R. and D.P.S. performed the analysis of XRD data by Rietveld refinement. A.X.B.Y., H.J. and E.E. performed the DFT calculations. Z.T., C.Z., K.T. and H.Y. assisted in sample preparation. A.P., H.A., P.V.B. and A.A.G. assisted with GITT and EIS measurements. H.A. assisted with preparation of schematics. W.C., J.-M.Z. and Q.C. wrote the manuscript. R.M.S., J.-M.Z. and Q.C. supervised the research. All authors contributed to the discussion of the results.

Competing interests

The authors declare no competing interests.

Additional information

Supplementary information The online version contains supplementary material available at <https://doi.org/10.1038/s41563-022-01381-4>.

Correspondence and requests for materials should be addressed to Jian-Min Zuo or Qian Chen.

Peer review information *Nature Materials* thanks Matthew McDowell and Colin Ophus for their contribution to the peer review of this work.

Reprints and permissions information is available at www.nature.com/reprints.